ChemComm

COMMUNICATION

View Article Online
View Journal | View Issue

Check for updates

Cite this: *Chem. Commun.*, 2025, 61, 9709

Received 15th March 2025,
Accepted 24th May 2025

DOI: 10.1039/d5cc01466b

rsc.li/chemcomm

Published on 26 May 2025. Downloaded by Shanghai Jiaotong University on 7/1/2025 12:41:15 PM.

Rational design of RuCu(P_xO_y) nanosheets for synergistically enhanced hydrogen evolution reaction in alkaline medium†

Haiyan Pang,[a] Zheng Tang,[a] Ruohan Huang,[a] Panpan Wang,[a] Xiao Liu, *[ab] Hongling Liu *[a] and Yuechang Wei *[c]

A robust catalyst of RuCu(P_xO_y) nanosheets is obtained by a simple hydrothermal method for alkaline HER. Structural analysis reveals that RuCu(P_xO_y) nanosheets are mainly composed of metallic Ru and amorphous Cu(P_xO_y), which can effectively accelerate electron transfer during the process of the HER. In alkaline electrolyte, the RuCu(P_xO_y) catalyst possesses a small overpotential of 67 mV (10 mA cm^{-2}) and Tafel slope of 90 mV dec^{-1}, which surpasses the Ru(P_xO_y), Cu(P_xO_y), and RuCu samples. In addition, such a catalyst for the HER can be extended to acidic media. This study is beneficial to the rational design of advanced efficient electrocatalysts for electrochemical HER in alkaline electrolytes.

The excessive dependence on fossil fuels has caused environmental problems, and hydrogen (H_2) has become attractive as a promising energy resource.[1–3] The production of high-purity and quality H_2 fuel by electrocatalytic water decomposition has developed into the primary emphasis of ongoing research and development.[4] However, unavoidable acid mist and erosion in the acidic electrolyte still limit its development in the industrial field.[5] The hydrogen evolution reaction (HER) under alkaline conditions is particularly intriguing for producing high-purity H_2 and has progressively emerged as a reliable and efficient technique in industrial applications.[6] Doubtless, the primary drawback of the HER in alkaline environments is its slow reaction kinetics, as extra energy is necessary to cleave the O–H bonds within water molecules.[7] Therefore, the creation of cost-effective HER electrocatalysts that exhibit high efficiency in alkaline environments is highly sought after, yet it continues to pose a significant challenge.

Among numerous advanced electrocatalysts, platinum (Pt) is widely regarded as the best catalyst for the HER, while its scarcity, high cost, and instability (undergo corrosion in alkaline media), hinder its feasibility for widespread commercial use.[8] Ruthenium (Ru) has surfaced as a viable substitute for Pt. Ru shares a similar hydrogen bond strength to Pt, making it highly effective for the HER, and it is significantly less expensive and more abundant, which addresses some of the key drawbacks of Pt in industrial applications.[9] To further reduce the cost of Ru-based catalysts, hybridizing Ru with another transition metal (especially Cu) is one of the most common strategies. Unexpectedly, the incorporation of transition metals presents a significant advantage by effectively lowering the energy barrier for the water dissociation process.[10]

Another strategy is to combine metal catalysts and heteroatoms (P, O, S, *etc.*). The interaction between heteroatoms and metal atoms modulates the d-band center position of active sites, optimizing the H* adsorption free energy to approach thermoneutrality ($\Delta G_H \approx 0$), thereby enhancing the HER kinetics.[11,12] In recent years, metal–O–P based catalysts have been extensively investigated in building novel catalytic systems.[13–15] The strong electronegativity of P, which bonds with the metal atom *via* O, drives electron transfer from the metal atom to the P–O unit. Such charge redistribution preferentially optimizes the H* desorption energetics at the metal sites.[16] Black phosphorus (BP), as a single-element P-based two-dimensional (2D) layered material, has sparked widespread focus.[17] The abundant lone-pair electrons on the surface of BP endow it with high reactivity, enabling the potential formation of P–O–metal bonds or P–metal bonds.[18] In addition, BP as a 2D support can also utilize metal catalysts as far as possible due to the excess availability of the anchor sites.[19] Such features are beneficial for improving HER performance in an alkaline medium.

In this work, we report a facile method for integrating Ru, Cu, and BP nanosheet compositions properly into a single

[a] *Henan Key Laboratory of Polyoxometalate Chemistry, College of Chemistry and Molecular Science, Henan University, Kaifeng 475001, P. R. China*
[b] *Henan Province Engineering Technology Research Center of Water Environment and Health, College of Pharmacy and Chemical Engineering, Zhengzhou University of Industrial Technology, Zhengzhou 451150, China*
[c] *State Key Laboratory of Heavy Oil Processing, China University of Petroleum, Chang Ping, Beijing 102249, China*

† Electronic supplementary information (ESI) available. See DOI: https://doi.org/10.1039/d5cc01466b

Published on 26 May 2025. Downloaded by Shanghai Jiaotong University on 7/1/2025 12:41:15 PM.

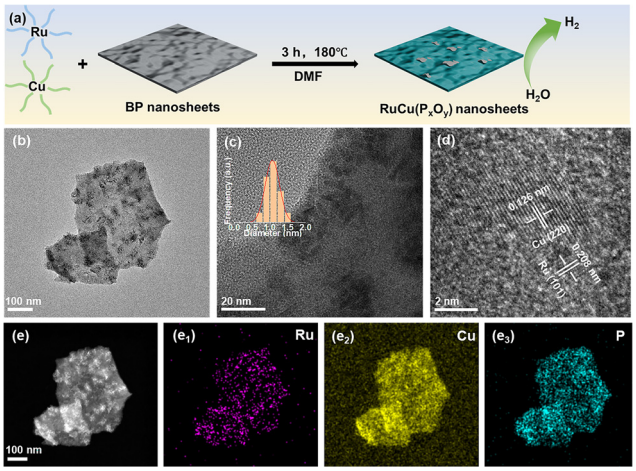

Fig. 1 (a) Schematic illustration of the synthesis of RuCu(P_xO_y) nanosheets. (b) TEM image of the RuCu(P_xO_y) nanosheet, (c) magnified TEM image, (d) HR-TEM image, and (e) HAADF-STEM and elemental mapping.

entity, namely RuCu(P_xO_y) nanosheets, with enhanced HER activity under alkaline media (Fig. 1a). Firstly, Ru precursor and Cu precursor were accumulated on the BP surface to form a complex. Subsequently, the RuCu(P_xO_y) nanosheets were obtained by further phosphating reaction under the solvothermal conditions. The synthesized materials (RuCu(P_xO_y), Ru(P_xO_y), Cu(P_xO_y), and RuCu) were directly used as HER catalysts in alkaline media. Obviously, the RuCu(P_xO_y) catalyst exhibited higher HER performance compared to other catalysts. In addition, the optimized RuCu(P_xO_y) catalyst possesses outstanding stability, exhibiting only a minimal potential shift during the 45-hour chronoamperometry test.

Bulk BP is obtained from red phosphorus using a straightforward low-pressure transport method.[20] Bulk BP and BP nanosheets are comprehensively characterized (Fig. S1 and S2, ESI†). Then, the BP nanosheets were further solvothermally treated in DMF solution containing Ru precursor and Cu precursor, yielding RuCu(P_xO_y) nanosheets. The morphology of the RuCu(P_xO_y) nanosheets was then investigated by transmission electron microscopy (TEM). Fig. 1b shows that the morphology of RuCu(P_xO_y) has a 2D nanostructure (the size of 310 ± 50 nm), and no discernible surface defects. Fig. 1c shows a TEM image of the enlarged area in Fig. 1b. Some tiny particles exhibit a nearly uniform and approximately spherical morphology with minimal aggregation on the surface of the RuCu(P_xO_y) nanosheet. The inset in Fig. 1c reveals the size distribution of tiny particles (average size: 1.08 ± 0.3 nm), which are well-fitted by the Gaussian function. In addition, the crystal lattice information of the RuCu(P_xO_y) nanosheets was investigated by high resolution TEM (HR-TEM). The HR-TEM image of a RuCu(P_xO_y) nanosheet is displayed in Fig. 1d. As marked, the lattice spacing of 1.26 Å aligns with the (220) crystal plane of metallic Cu. The element distribution of the RuCu(P_xO_y) nanosheet surface was further analyzed by high-angle annular dark field scanning transmission electron microscopy (HAADF-STEM). As shown in Fig. 1e, the elements Ru, Cu, and P were uniformly distributed, indicating the successful synthesis of RuCu(P_xO_y) nanosheets.

To further verify the amorphous state of phosphide in the RuCu(P_xO_y) nanosheets, the X-ray diffraction (XRD) pattern was collected (Fig. S3, ESI†). The diffraction peaks located at 43.2°, 50.4°, and 74.1° are allocated to the (111), (200), and (220) diffraction planes of Cu (JCPDS No. 04-0836), demonstrating that a small amount of metallic Cu is present in the RuCu(P_xO_y) nanosheets,[21] which was further confirmed *via* X-ray photoelectron spectroscopy (XPS) in the below. Whereas, there are no BP diffraction peaks observed for the Ru(P_xO_y), Cu(P_xO_y), and RuCu(P_xO_y) nanosheets, suggesting that the highly crystalline BP is transformed into amorphous phosphorus oxide after solvothermal treatment. The elemental makeup and surface chemical properties of the Ru(P_xO_y), Cu(P_xO_y), and RuCu(P_xO_y) nanosheets were studied by XPS. The high-resolution spectrum of Ru 3p is shown in Fig. 2a. The two distinct peaks of the RuCu(P_xO_y) sample around 461.7 eV and 483.7 eV are fitted to Ru $3p_{3/2}$ and Ru $3p_{1/2}$,[22] which slightly shift toward lower energy compared with those of the Ru(P_xO_y) sample (462.1 eV and 484.3 eV). Such a peak shift is mainly because of electron density from Cu to Ru due to the difference in electronegativity (Ru:2.2; Cu:1.9). The enhanced electron density around the Ru induces strong attractive interactions with the inner layer, causing a shift of binding energy. The peaks at 463.8 eV and 485.7 eV for the RuCu(P_xO_y) sample could be attributed to Ru^{4+}.[23] Apart from the Ru 3p spectrum, the high-resolution spectrum of Cu 2p for the RuCu(P_xO_y) sample was exhibited, which reveals the coexistence of Cu^0, Cu^{1+}, and Cu^{2+} (Fig. 2b). In detail, the major peaks at 934.3 eV and 954.4 eV are still ascribed to Cu^{2+}, and at 932.1 eV and 952.3 eV are assigned to Cu^{1+}, suggesting that Cu exists in a mixed valence state on the surface of RuCu(P_xO_y).[24] The binding energy at 931.2 eV and 950.7 eV is assigned to Cu^0.[25] Inversely, the main Cu 2p peaks undergo a minor shift toward higher binding energy relative to the Cu(P_xO_y) sample (934.7 eV and 954.7 eV). In addition, the peak appearing around 133.02 eV can be attributed to the P–O for Ru(P_xO_y),[20] as shown in Fig. 2c. Owing to P–O and Cu interaction, this peak appears at the lower binding energy for the Cu(P_xO_y) (132.68 eV) and RuCu(P_xO_y) (132.70 eV) samples. Based on XPS data, the Ru element and Cu element are mainly in the form of Ru^0 (87.2%) and Cu(P_xO_y) (93.1%) in the Ru 3p and Cu 2p core-level XPS spectra, respectively. Hence, we deduce that the synergistic effect between Ru and amorphous Cu(P_xO_y) is a key factor in enhancing the HER activity.

To assess electrocatalytic performance, various catalyst electrodes were evaluated by utilizing a conventional three-electrode configuration at 1.0 M KOH. Firstly, the ratio of Ru precursor

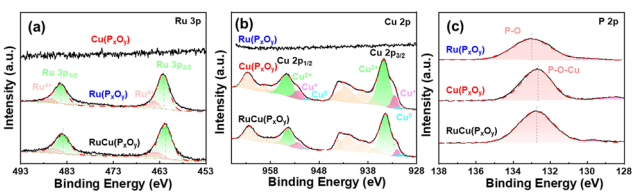

Fig. 2 XPS spectra of analyses of the RuCu(P_xO_y) nanosheets. (a) Ru 3p HR-XPS spectra, (b) Cu 2p HR-XPS spectra, and (c) P 2p HR-XPS spectra.

This journal is © The Royal Society of Chemistry 2025

Published on 26 May 2025. Downloaded by Shanghai Jiaotong University on 7/1/2025 12:41:15 PM.

and Cu precursor, as well as the amount of BP support was investigated (Fig. S4 and S5, ESI†). Based on HER performance, the optimized ratio (Ru : Cu) and amount of BP have been determined to be 1 : 2 and 5 mg, respectively. Thereafter, samples of Ru(P_xO_y), Cu(P_xO_y), RuCu, and RuCu(P_xO_y) catalysts were subsequently evaluated under identical conditions. The LSV polarization curves for the HER of all the samples with a low scan rate at 2 mV s^{-1} are illustrated in Fig. 3a. The RuCu(P_xO_y) catalyst exhibits the most superior HER activity with ultralow overpotentials at 10 mA cm^{-2} of 67 mV, while the overpotentials at 10 mA cm^{-2} of the Ru(P_xO_y), Cu(P_xO_y), and RuCu catalyst are 301 mV, 319 mV, and 335 mV, respectively (Fig. 3b). Similarly, the overpotentials at 100 mA cm^{-2} of the RuCu(P_xO_y) catalyst are only 265 mV for the HER, which is also much lower than that of Ru(P_xO_y), Cu(P_xO_y), and RuCu (721 mV, 598 mV, and 691 mV, respectively). This result is close to those of commercial Pt/C (20 wt%). Moreover, electrocatalytic stability serves as another crucial criterion for evaluating the performance of catalysts. The durability of the RuCu(P_xO_y) nanosheets was validated *via* chronoamperometry testing at −1.065 V (Fig. S6, ESI†). The catalyst retains nearly the same initial current density following 45 h of continuous operation in an alkaline medium, showing the robust durability of the RuCu(P_xO_y) catalyst. Based on the excellent performance toward the HER, the overall water splitting measurements were accomplished in a two-electrode system, where the commercial RuO_2 acts as an anode and RuCu(P_xO_y) acts as a cathode in an alkaline medium. The RuO_2 (+)‖RuCu(P_xO_y) (−) electrolyzer operates with a potential of 2.43 V to achieve a current density of 10 mA cm^{-2} (Fig. S7, ESI†). It is noted that the catalysts on the electrode surface would undergo irreversible surface reconstruction during the HER process in the alkaline medium (Fig. S8–S10, ESI†).

The Tafel slope is a significant parameter for revealing the reaction mechanism and examining the HER kinetics by illustrating the dependence of overpotential on current density.[26] The Tafel slope of RuCu(P_xO_y) (90 mV dec^{-1}) is lower than that of Ru(P_xO_y) (246 mV dec^{-1}), Cu(P_xO_y) (162 mV dec^{-1}), and RuCu (244 mV dec^{-1}), suggesting the faster electron transfer on the RuCu(P_xO_y) nanosheet surface (Fig. 3c). At the same time, RuCu(P_xO_y) proceeds along the Volmer–Heyrovsky mechanism during the HER reaction, and the electrochemical hydrogen adsorption process acts as the rate-determining step.[27] In addition, the superior HER performance of RuCu(P_xO_y) surpassed those of similar catalysts in recently reported literature (Table S1, ESI†). For desirable electrocatalysts, the HER catalytic performance under an acidic medium is very attractive. Given this, the HER activities of the RuCu(P_xO_y) catalysts were also performed in 0.5 M H_2SO_4 solution (Fig. S11 and S12, ESI†). As expected, RuCu(P_xO_y) is a favorable HER electrocatalyst with an overpotential of 83 mV at a current density of 10 mA cm^{-2}, which is considerably lower than that of Ru(P_xO_y) (151 mV), Cu(P_xO_y) (375 mV), and RuCu (144 mV). Simultaneously, RuCu(P_xO_y) nanosheets manifest lower Tafel slopes of 77 mV dec^{-1} for the HER as compared with Ru(P_xO_y) (181 mV dec^{-1}), Cu(P_xO_y) (275 mV dec^{-1}), and RuCu (103 mV dec^{-1}). The smaller Tafel slope combined with low overpotential demonstrates that RuCu(P_xO_y) nanosheets are also outstanding HER electrocatalysts in acidic solutions, outperforming most reported state-of-the-art Ru-based electrocatalysts (Table S2, ESI†). In addition, the HER catalytic performance of Ru + Cu(P_xO_y) (physical mixing) was investigated to suggest a synergistic effect of the two phases (Fig. S13, ESI†). The effect of types of P precursors in the RuCu(P_xO_y) catalysts on catalytic activity was explored to verify the importance of the P element (Fig. S14–S16, ESI†).

Based on previous research,[28,29] we anticipated the entire process of the HER (Fig. 4a). Firstly, a water molecule is chemically absorbed on the Ru active site (Ru–H_2O) of the catalyst surface, then acquires an electron to form Ru–OH* and a Cu–H* intermediate (H_2O + Ru + Cu + e^- → Cu–H* + Ru–OH*). Theoretically, Cu active sites are more prone to H* desorption relative to Ru active sites.[30] Ultimately, two adjacent active intermediates Cu–H* generate H_2 (Cu–H* + Cu–H* → 2Cu + H_2). During this process, P–O units can also modulate the electronic structure of Cu sites, promoting the desorption of H*.[31] Subsequently, turnover frequency (TOF) normalized per active site was employed to assess the catalytic activity of RuCu(P_xO_y),[32] as shown in Fig. 4b. Significantly, the TOF values of the RuCu(P_xO_y) catalyst (0.0471 s^{-1}, 0.0676 s^{-1} and 0.0888 s^{-1}) were higher than those of the Ru(P_xO_y) (0.0013 s^{-1}, 0.0029 s^{-1} and 0.0049 s^{-1}), Cu(P_xO_y) (0.00007 s^{-1}, 0.0009 s^{-1} and 0.0026 s^{-1}), and RuCu (0.0010 s^{-1}, 0.0022 s^{-1} and 0.0042 s^{-1}) catalysts at

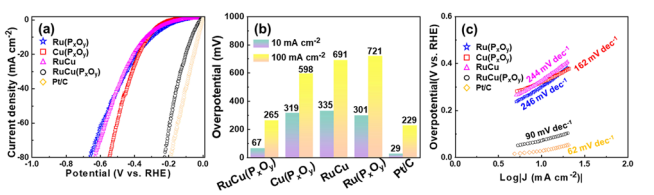

Fig. 3 HER performances of different catalysts (Ru(P_xO_y), Cu(P_xO_y), RuCu, RuCu(P_xO_y), Pt/C) in an alkaline medium. (a) LSV curves, (b) overpotential at 10 and 100 mA cm^{-2} for the HER, and (c) Tafel plots.

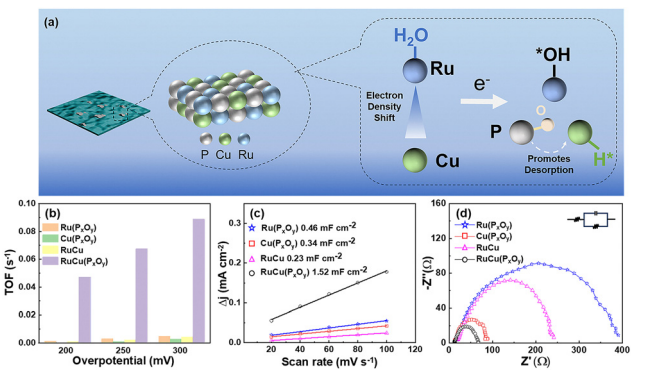

Fig. 4 (a) Schematic of the HER mechanism on the RuCu(P_xO_y) nanosheets in alkaline conditions. (b) TOF of different catalysts, (c) the linear fit of the capacitive currents of the catalysts *versus* potential scanning rates from 20 mV s^{-1} to 100 mV s^{-1}, and (d) Nyquist plots of the electrochemical impedance spectra of different catalysts.

Published on 26 May 2025. Downloaded by Shanghai Jiaotong University on 7/1/2025 12:41:15 PM.

three selected potentials (200 mV, 250 mV, 300 mV), revealing the highest intrinsic catalytic activity of the RuCu(P_xO_y) catalyst.

To further understand the intrinsic features of the catalytic material, the fundamental mechanism behind the enhanced HER performance of the RuCu(P_xO_y) was investigated by electrochemically active surface area (ECSA) and electrochemical impedance spectroscopy (EIS) analysis. Typically, the number of catalytically active sites can be assessed by the ECSA, which is directly proportional to the double-layer capacitance (C_{dl}) (Fig. S17, ESI†). The ECSA shows that the C_{dl} of the RuCu(P_xO_y) (9.03 mF cm^{-2}) is larger than that of the Ru(P_xO_y) (7.97 mF cm^{-2}), Cu(P_xO_y) (6.29 mF cm^{-2}), and RuCu (2.29 mF cm^{-2}), indicating that the RuCu(P_xO_y) provides a greater number of accessible catalytically active sites (Fig. 4c). The resistance in the electrode/electrolyte interface for charge transfer was assessed *via* EIS tests (Fig. 4d). Based on the analytical results, the R_{ct} of RuCu(P_xO_y) is 19.11 Ω, while the R_{ct} values of Ru(P_xO_y) (91.55 Ω), Cu(P_xO_y) (27.15 Ω), and RuCu (72.07 Ω) are obviously larger than that of RuCu(P_xO_y). The lowest R_{ct} value of RuCu(P_xO_y) nanosheets exhibits a more rapid electron transport and promising HER kinetics, matching the low overpotential and small Tafel slope.

In summary, a sample strategy was proposed to prepare the RuCu(P_xO_y) with a stable 2D structure and enhanced HER performance under alkaline media. The optimal RuCu(P_xO_y) catalyst presents a low overpotential (67 mV) at 10 mA cm^{-2}, small Tafel slope (90 mV dec^{-1}), and persistent stability. At the same time, the outstanding performance for the HER can also be extended to acidic media. Mechanism analysis indicates that the superior performance of the HER is attributed to the synergistic effect between metallic Ru and amorphous Cu(P_xO_y). This study offers promising potential for the advancement of Ru-based catalysts in energy storage and conversion applications.

This work was supported in part by the National Science Foundation of China (No. 51172064) and the Natural Science Foundation of Henan Province (232300420369; 242300420533).

Data availability

The data supporting this article have been included as part of the ESI.†

Conflicts of interest

The authors declare that they have no competing interests.

Notes and references

1 M. S. Dresselhaus and I. L. Thomas, *Nature*, 2001, **414**, 332–337.
2 C. Shi, X. Li, W. Yang, X. Liu, Y. An, L. Zhou and L. Mai, *Chem. Commun.*, 2022, **58**, 5269–5272.
3 D. Wu, H. Du, Z. Liu, G. Bagliu, J. Lai and L. Wang, *EcoEnergy*, 2024, **2**, 724–735.
4 Y. Gu, N. Nie, J. Liu, Y. Yang, L. Zhao, Z. Lv, Q. Zhang and J. Lai, *EcoEnergy*, 2023, **1**, 405–413.
5 J. W. Huang, W. T. Hong and W. Liu, *Appl. Surf. Sci.*, 2022, **579**, 152152.
6 X. Liu, X. Wang, K. Li, J. Tang, J. Zhu, J. Chi, J. Lai and L. Wang, *Angew. Chem., Int. Ed.*, 2024, **136**, e202316319.
7 P. Z. Chen, K. Xu, S. Tao, T. P. Zhou, Y. Tong, H. Ding, L. D. Zhang, W. S. Chu, C. Z. Wu and Y. Xie, *Adv. Mater.*, 2016, **28**, 7527–7532.
8 H. Li, Y. Han, H. Zhao, W. Qi, D. Zhang, Y. Yu, W. Cai, S. Li, J. Lai and B. Huang, *Nat. Commun.*, 2020, **11**, 5437.
9 S. Y. Wang, X. R. Ning, X. H. Liu, M. Shakouri, Y. F. Hu, H. Y. Yuan, P. F. Liu, X. Y. Lu, Y. Guo and Y. Q. Wang, *Carbon*, 2024, **217**, 118611.
10 D. Cao, J. Y. Wang, H. X. Xu and D. J. Cheng, *Small*, 2020, **16**, 2000924.
11 L. Wang, W.-W. Tian, W. Zhang, F. Yu and Z.-Y. Yuan, *Appl. Catal., B*, 2023, **338**, 123043.
12 S. Jiao, X. Fu and H. Huang, *Adv. Funct. Mater.*, 2022, **32**, 2107651.
13 Y. Yuan, K. Wang, B. Zhong, D. Yu, F. Ye, J. Liu, J. Dutta and P. Zhang, *Energy Environ. Sci.*, 2024, **7**, e12747.
14 B. Chong, M. Xia, Y. Lv, H. Li, X. Yan, B. Lin and G. Yang, *Chem. Eng. J.*, 2023, **465**, 142853.
15 X. Chen, Z. Wang, D. Luo, R. Hu, Y. Cui, J. Gao, B. Dai and C. Xu, *Surf. Interfaces*, 2024, **52**, 104847.
16 K. A. Moltved and K. P. Kepp, *J. Phys. Chem. C*, 2019, **123**, 18432–18444.
17 X. Liu, P. Fan, L. Xiao, J. Weng, Q. Xu and J. Xu, *J. Energy Chem.*, 2021, **53**, 185–191.
18 X. Liu, L. Xiao, J. Weng, Q. Xu, W. Li, C. Zhao, J. Xu and Y. Zhao, *Sci. Adv.*, 2020, **6**, eabb4359.
19 Z. Zhao, H. Liu, W. Gao, W. Xue, Z. Liu, J. Huang, X. Pan and Y. Huang, *J. Am. Chem. Soc.*, 2018, **140**, 9046–9050.
20 X. Liu, Y. F. Bai, J. Xu, Q. C. Xu, L. P. Xiao, L. P. Sun, J. Weng and Y. L. Zhao, *Adv. Sci.*, 2019, **6**, 1901991.
21 J. X. Liu, G. Y. Ning, K. Shi, M. Zheng, Y. N. Sun, Y. J. Gao, Y. F. Zhang and H. Wang, *Int. J. Hydrogen Energy*, 2022, **47**, 5947–5960.
22 G. Meng, H. Tian, L. X. Peng, Z. H. Ma, Y. F. Chen, C. Chen, Z. W. Chang, X. Z. Cui and J. L. Shi, *Nano Energy*, 2021, **80**, 105531.
23 W. H. Feng, Y. Q. Feng, Y. R. He, J. S. Chen, H. Wang, T. M. Luo, Y. Z. Hu, C. K. Yuan, L. Y. Cao and L. L. Feng, *Inorg. Chem. Front.*, 2022, **9**, 4151–4159.
24 N. Wang, X. He, Y. J. Chen, B. L. Sun, X. C. Xie, S. W. Koh, L. X. He and M. Q. Yao, *J. Porous Mater.*, 2021, **28**, 763–771.
25 H. C. Liu, F. Yang, Z. S. Xu, X. R. Yan, F. J. Chen, C. Xu, S. Che and Y. F. Li, *Electrochim. Acta*, 2022, **430**, 141075.
26 S. X. Bai, M. Xie, T. Cheng, K. L. Cao, Y. Xu and X. Q. Huang, *Nano Energy*, 2020, **78**, 105224.
27 W. X. Wang, Q. Q. Mao, K. Deng, H. J. Yu, Z. Q. Wang, Y. Xu, X. N. Li, L. Wang and H. J. Wang, *Small*, 2023, **19**, 2207852.
28 M. Ďurovič, J. Hnát and K. Bouzek, *J. Power Sources*, 2021, **493**, 229708.
29 H. Zhang, J. Diao, Y. Liu, H. Zhao, B. K. Ng, Z. Ding, Z. Guo, H. Li, J. Jia and C. Yu, *Adv. Mater.*, 2023, **35**, 2305742.
30 J. Wang, B. Guo, J. Sun, Y. Zhou, C. Zhao, Z. Wei and J. Guo, *Appl. Catal., B*, 2023, **324**, 122169.
31 C. Lyu, C. Cao, J. Cheng, Y. Yang, K. Wu, J. Wu, W.-M. Lau, P. Qian, N. Wang and J. Zheng, *Chem. Eng. J.*, 2023, **464**, 142538.
32 J. N. Hansen, H. Prats, K. K. Toudahl, N. Mørch Secher, K. Chan, J. Kibsgaard and I. Chorkendorff, *ACS Energy Lett.*, 2021, **6**, 1175–1180.

 This journal is © The Royal Society of Chemistry 2025